Computational Imaging with Dynamically Reconfigurable Metasurface Antennas: An Experimental Study

Amir Masoud Molaei
Centre for Wireless Innovation
Queen's University Belfast
Belfast, U.K.
a.molaei@qub.ac.uk

María García-Fernández
Group of Signal Theory and Communications
University of Oviedo
Gijón, Spain
garciafmaria@uniovi.es

Guillermo Álvarez-Narciandi
Group of Signal Theory and Communications
University of Oviedo
Gijón, Spain
alvareznguillermo@uniovi.es

Okan Yurduseven
Centre for Wireless Innovation
Queen's University Belfast
Belfast, U.K.
okan.yurduseven@qub.ac.uk

***Abstract*—This paper presents an experimental study on computational imaging (CI) using dynamically reconfigurable metasurface antennas (DMAs). By leveraging DMAs, the system generates spatially incoherent radiation patterns (measurement modes), enabling efficient three-dimensional image reconstruction with reduced hardware complexity. The performance of the proposed system is evaluated through experimental tests, analyzing key factors such as the number of tuning states (i.e., the number of masks), the number of frequency samples, and the image reconstruction methods. The results demonstrate that increasing the number of masks and frequency samples enhances the image quality while reducing them leads to degraded reconstruction performance. Furthermore, we conduct a comparative study between two spatial reconstruction techniques, namely matched-filter and least-squares, using the synthesized DMA system, providing a trade-off in terms of the computational efficiency and the image reconstruction quality. The findings confirm that DMA-based CI systems offer a flexible and hardware-efficient solution for electromagnetic imaging, paving the way for advanced applications in security screening, biomedical imaging and non-destructive testing.**

***Keywords*—Computational imaging, dynamic metasurface antennas, experimental results, image reconstruction.**

I. INTRODUCTION

Electromagnetic imaging technologies have been widely adopted for various applications, including security screening, medical diagnostics, environmental monitoring and non-destructive testing to name a few [1], [2], [3], [4], [5]. Traditional imaging techniques, such as synthetic aperture radar and phased array systems [6], [7], require either mechanically scanned apertures or a significant number of transmitters (TXs) and receivers (RXs) to achieve high-resolution imaging. These approaches, while effective, impose limitations in terms of hardware complexity, cost and data acquisition time [8]. To address these challenges, computational imaging (CI) techniques [9], [10] have emerged as an alternative, leveraging advanced aperture designs and signal processing techniques to extract spatial information from a reduced number of measurements.

This work was supported by Leverhulme Trust under the Research Leadership Award under Grant RL-2019-019. The work of M. García Fernández and G. Álvarez-Narciandi was also supported by MICIU/AEI/10.13039/501100011033 and by ESF+ under grants RYC2023-043020-I and RYC2023-045010-I, respectively.

A key enabler of CI is the use of dynamically reconfigurable metasurface antennas (DMAs) [11], [12], which offer a flexible and hardware-efficient alternative for generating spatially incoherent radiation patterns. Unlike conventional phased arrays that rely on phase shifters and multiple radio frequency chains, DMAs utilize tunable metamaterial elements to reconfigure their radiation patterns dynamically [11]. This allows for significant reductions in power consumption and system complexity while maintaining the ability to synthesize large effective apertures [13]. Recent advancements in DMA-based CI systems have demonstrated their potential for achieving high-resolution three-dimensional (3D) imaging with minimal hardware requirements [13], [14], [15], [16], [17].

One promising approach to DMA-based CI involves configurations based on employing two 1D DMAs (orthogonally in a Mills Cross structure [16], [18] or an L-shaped structure [19]) arranged to synthesize a 2D effective aperture. These configurations maximize spatial sampling efficiency while reducing hardware complexity. The use of multiple tuning states, or *masks* [13], further enhances spatial diversity, allowing the system to encode and retrieve scene information more effectively. While previous works have explored various CI frameworks using metasurface antennas, experimental validation of DMA-based systems and their systematic analyses as a function of different system parameters remains understudied.

In this paper, we present an experimental investigation into CI using DMAs configured in an L-shaped arrangement. We describe the implementation of a DMA-based imaging system and evaluate its performance in retrieving target images. Through a systematic analysis of key system factors, including the number of masks, the number of frequency samples, the frequency bandwidth, and the image reconstruction algorithm, we assess the trade-offs between image quality and processing time. Our results demonstrate the effectiveness of the proposed system in achieving efficient microwave imaging and highlight the potential of DMAs for next-generation CI applications.

The rest of this paper is organized as follows. In Section II, the system model is introduced. Section III describes the image reconstruction mechanism. In Section IV, the results of experimental studies using the CI system introduced in this

paper are presented and discussed. Finally, Section V is devoted to the conclusion.

II. System Model

The CI system in this study utilizes two DMAs arranged in an L-shaped configuration to maximize spatial sampling efficiency (see Fig. 1). One of these DMAs functions as the TX, while the other one serves as the RX. Each DMA consists of sub-wavelength-sized metamaterial elements with their radiation response being controlled in a binary fashion, *on* or *off*, using diodes. During operation, the TX and RX DMAs cycle through a series of diode configurations, which modulate their radiation patterns. At a given time, each DMA aperture configuration, with a specific pattern of *on*/*off* element tuning states, constitutes a *mask*. This enables the system to acquire scene information through $M = m_{\mathrm{T}} m_{\mathrm{R}} m_{\mathrm{f}}$ measurement modes, where m_{T}, m_{R} and m_{f} represent the number of TX masks, the number of RX masks, and the number of sampled frequency points, respectively.

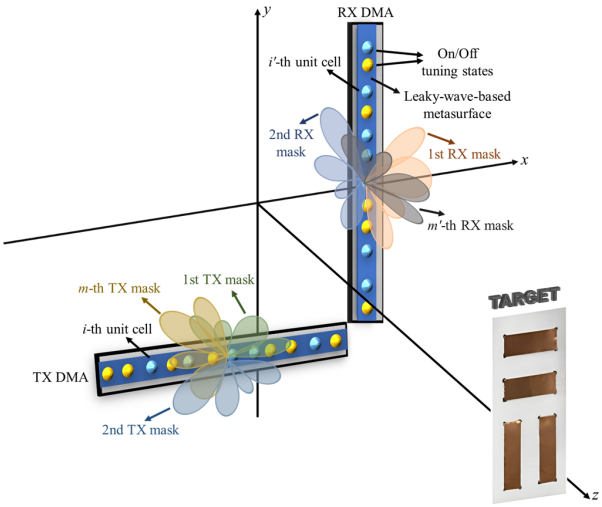

Fig. 1. General schematic of the imaging system. The DMAs aperture and the target are assumed to be located in the $z = 0$ and $z = z_0 > 0$ planes, respectively. A picture of the actual imaging setup (experimental setup) is available in Fig. 4 of [19].

The TX and RX DMAs consist of n_{T} and n_{R} non-uniformly spaced (sparse) unit cells, respectively, which are linearly distributed. This sparsity optimizes imaging capabilities while reducing hardware complexity [20]. Each unit cell is controlled (to be turned *on* and *off*) using a PIN diode, allowing for dynamic modification of the radiation pattern. To synthesize the DMA aperture, different unit cell topologies can be used (without loss of generality), including a variant of a circular complementary electric inductive-capacitive element structure [19], which is also used in this work.

III. Image Reconstruction

Mathematically, the interaction between the transmitted and received fields with the scene reflectivity is governed by the first Born approximation [21], which assumes weak scattering and linearizes Maxwell's equations. Under this approximation, the backscattered signal at the receiver, denoted as $\mathbf{g}$, is given by [13]

$$\mathbf{g}_{M\times 1} = \mathbf{H}_{M\times N}\boldsymbol{\rho}_{N\times 1} + \mathbf{w}_{M\times 1}, \tag{1}$$

where $\mathbf{H}$ represents the system's sensing matrix, defined by the dot product of the fields radiated by the TX and RX antennas (i.e., $\mathbf{H} \propto \mathbf{E}^{\mathrm{TX}}_{M\times N} \cdot \mathbf{E}^{\mathrm{RX}}_{M\times N}$) [22]. The scene's reflectivity, $\boldsymbol{\rho}$, is discretized into N voxels, and $\mathbf{w}$ represents system noise.

To reconstruct a 3D image of the scene, an estimate of the reflectivity distribution, $\hat{\boldsymbol{\rho}}$, is obtained by solving an inverse problem. A commonly employed method is the least-squares (LS) estimation, which minimizes the following cost function [23], [24]:

$$\hat{\boldsymbol{\rho}} = \arg\min_{\boldsymbol{\rho}} \left\| \mathbf{g} - \mathbf{H}\boldsymbol{\rho} \right\|_2^2, \tag{2}$$

where $\|\cdot\|_2$ denotes the Euclidean norm. Due to the ill-posed nature of the inverse problem, regularization techniques such as Tikhonov regularization [25], sparsity constraints [26], or iterative solvers like the generalized minimum residual (GMRES) method [27] can be incorporated to enhance reconstruction accuracy and robustness against noise.

An alternative reconstruction approach is the matched filter (MF), which is a single-shot reconstruction technique known for its robustness against noise. The MF solution is given by [28]

$$\hat{\boldsymbol{\rho}} = \mathbf{H}^H \mathbf{g}, \tag{3}$$

where superscript $(\cdot)^H$ denotes the conjugate transpose. The MF technique is computationally efficient and provides rapid image reconstruction, making it suitable for real-time applications. However, it may suffer from lower resolution compared to more sophisticated iterative techniques like LS reconstruction with regularization.

IV. Experimental Results and Discussion

In this section, the experimental results obtained by the CI system are presented and the parameters affecting the final outputs are discussed. All computations have been done on MATLAB R2022a running on a 64-bit Windows Server 2019 operating system with 256 GB of random-access memory (RAM), a Xeon central processing unit (CPU) at 3.6 GHz, and an NVIDIA RTX A6000 graphics processing unit (GPU) with 48 GB memory. Unless specified otherwise, each experiment utilized $m_{\mathrm{T}} m_{\mathrm{R}} = 15\times 15$ masks and $m_{\mathrm{f}} = 51$ frequency points uniformly distributed across the operating bandwidth of the fabricated DMAs (i.e., 18 to 20 GHz). This setup provided a total of 11,475 measurement modes, ensuring a comprehensive dataset for image reconstruction. To synthesize the DMA-based CI system, the fabricated DMA panels presented in [19] were used. The length of the antennas is 24.5 cm. A microcontroller board, interfaced with four 8-bit shift registers, governs the activation of diodes, dynamically altering the masks for both DMAs. The masks are randomly generated with an activation probability of $p_{on} = 0.5$. The

fields radiated at different frequencies by the different masks of each DMA, which must be characterized to compute the sensing matrix of the CI system, were measured in planar grids of 3233 spatial points at $z = 10\,\text{cm}$ using an open-ended waveguide probe. The experiments involve imaging a target consisting of 4 copper stripes with sizes $7.5\,\text{cm} \times 2\,\text{cm}$ (2 horizontal and 2 vertical), as shown in Fig. 1, located at $z_0 = 33\,\text{cm}$. The number of voxels considered to form the scene is $N = n_x n_y n_z = 58 \times 58 \times 11$; and the size of each voxel is $4.5\,\text{mm} \times 4.5\,\text{mm} \times 20\,\text{mm}$. For image reconstruction, both the MF and LS techniques are used (as presented in Section III). In the case of the LS reconstructions, the GMRES iterative solver [29] is used.

Fig. 2 shows the reconstructed image of the scene at $z = 33\,\text{cm}$ (xy cross-sectional cut of the resulting 3D image at the range where the target is located) using the GMRES method with $n_i = 30$ iterations. In this figure, the positions of the TX and RX DMAs are marked with white dotted lines. The positions of the stripes are also outlined with white solid lines. It can be seen that in the reconstructed image, all four stripes can be identified in their correct positions. The processing times for implementing the image reconstruction technique on the CPU and GPU were 50.6 and 2.65 seconds, respectively. The computation time for constructing the sensing matrix on the CPU was 32.57 hours. Note that the computations related to constructing the sensing matrix are usually not considered part of the online (pure) processing; because it is independent of the target and depends only on the setup of the imaging system and the dimensions of the scene. Therefore, as long as the setup of the imaging system (including all parameters related to the TX and RX, and their positions) and the dimensions of the scene (including the position and size of the voxels) are fixed, the computations related to constructing the sensing matrix need to be carried out only once and can be done offline.

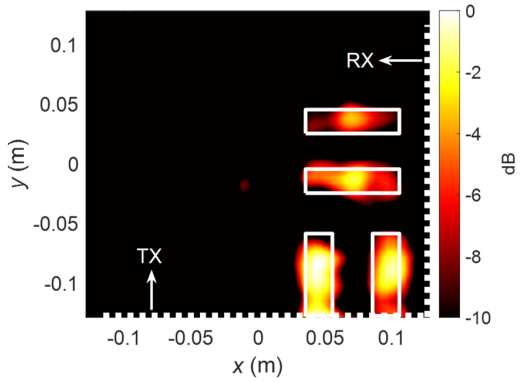

Fig. 2. Reconstructed image of the target at $z = 33\,\text{cm}$ using the LS method with $n_i = 30$.

In Fig. 3, a comparison between the reconstructed images by the MF method and the LS method (with different numbers of iterations) is presented. In general, it can be qualitatively observed that the LS technique provides a better quality image (objects are better identified). It can also be deduced that increasing the number of iterations leads to an improvement in the quality of the images. This can also be investigated quantitatively, with the normalized mean squared error (NMSE) criterion [30], the results of which are given in Table I. By considering Fig. 2 as a reference image, it can be seen from Table I how the choice of the algorithm and its parameters can affect the final result. However, the improvement in the above results comes at the cost of increasing the computational cost. In Table I, the processing time corresponding to each image on both CPU and GPU is given. It is obvious that the GPU, due to its inherently massively parallel architecture, has increased the processing speed. This improvement is more noticeable in the case of heavier calculations.

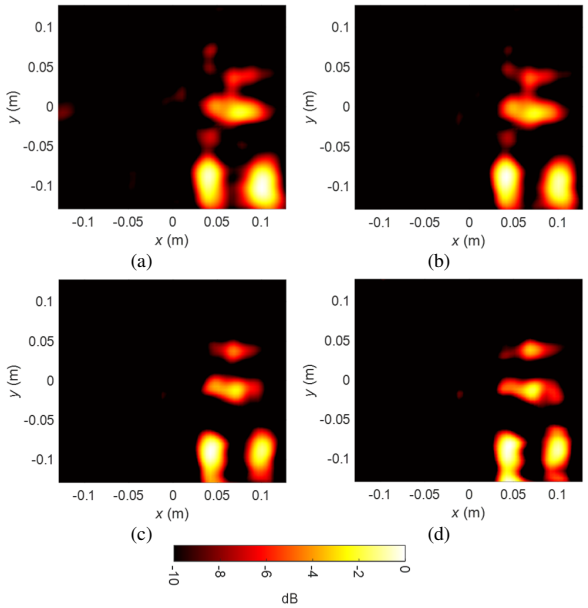

Fig. 3. Reconstructed image of the target at $z = 33\,\text{cm}$, and with $m_T = m_R = 15$; (a) using the MF method, (b) using the LS method with $n_i = 2$, (c) using the LS method with $n_i = 10$, (d) using the LS method with $n_i = 30$.

To investigate the effect of the number of masks on the final result, the number of TX and RX masks, m_T and m_R, was reduced from 15 to 10 and then to 5. The obtained reconstructed images are shown in Fig. 4. Compared to the corresponding images in Fig. 3, it can be seen that the quality of the reconstructions decreased as the number of masks was reduced. This can also be verified by examining the NMSE data in Table I. As a result, it can be deduced that increasing the number of masks, which leads to a significant increase in the number of measurements, improves the quality of the final images. From the data in Table I, it can be seen that, unlike the MF method, reducing the number of measurements did not have a significant effect on reducing the processing time when using the LS method. The reason for this is that the size of input matrices and vectors of the image reconstruction algorithm based on the GMRES technique is mainly affected by the number of voxels rather than the number of measurements. However, reducing the number of

measurements speeds up the data acquisition process. Also, the time needed for constructing the sensing matrix on the CPU was reduced to 14.2 and 3.55 hours for $m_T = m_R = 10$ and $m_T = m_R = 5$, respectively.

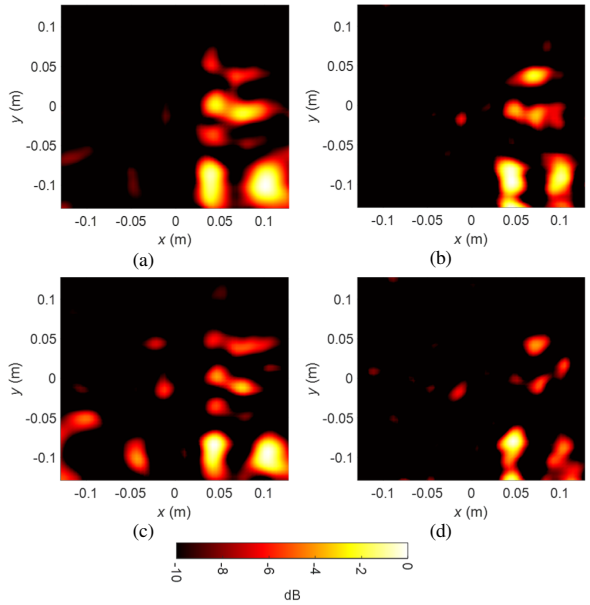

Fig. 4. Reconstructed image of the target at $z = 33\text{cm}$; (a) using the MF method, and $m_T = m_R = 10$, (b) using the LS method with $n_i = 30$, and $m_T = m_R = 10$, (c) using the MF method, and $m_T = m_R = 5$, (d) using the LS method with $n_i = 30$, and $m_T = m_R = 5$.

TABLE I. COMPARISON OF NMSE VALUES AND PROCESSING TIMES CORRESPONDING TO THE RECONSTRUCTED IMAGES IN FIGS. 3 AND 4

Figure	NMSE	Processing time on CPU (Sec)	Processing time on GPU (Sec)
3(a)	0.32	0.33	0.035
3(b)	0.25	4.03	0.43
3(c)	0.052	17.25	1.03
3(d)	0	50.6	2.48
4(a)	0.36	0.13	0.019
4(b)	0.11	50.03	2.46
4(c)	0.41	0.038	0.024
4(d)	0.37	49.36	2.52

To examine the reconstructed image along the range (z-axis), Figs. 5(a) and 5(b) are extracted, corresponding to the output of the MF method and the LS method, respectively. It can be seen that the highest normalized powers, i.e., the range of 0 to -2 dB (bright areas), are concentrated around the true range of the target. Hence, it can be concluded that the synthesized DMA-CI system can successfully retrieve the location of the imaged target using both the MF and LS reconstructed techniques within the operating frequency band (18-20 GHz) sampled at $m_f = 51$ frequency points.

In the final experiment, the effect of reducing the bandwidth and the number of frequency samples, m_f, on the results is investigated. Fig. 6 demonstrates the reconstructed images in the xy and xz planes using the MF and LS methods when the measurements include 26 frequency samples uniformly distributed in the frequency band 18-19 GHz. Compared to the images in Fig. 3, it is observed that the reduction in the number of frequency samples, which is equivalent to a significant reduction in the total number of measurements, has resulted in almost one of the stripes (the upper stripe) not being identifiable. Also, compared to the image in Fig. 5, it is observed that in Figs. 6(c) and 6(d), sidelobes are dominant; so that it is not possible to extract the target range by visual inspection. Also, the reduction of bandwidth has led to the loss of range resolution. The calculated NMSE values corresponding to the reconstructed images by the MF and LS methods in Fig. 6 are 0.4 and 0.14, respectively.

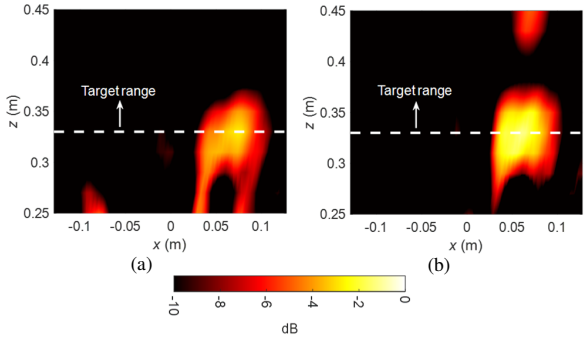

Fig. 5. Reconstructed image of the target at $y = 0$; (a) using the MF method, (b) using the LS method with $n_i = 30$.

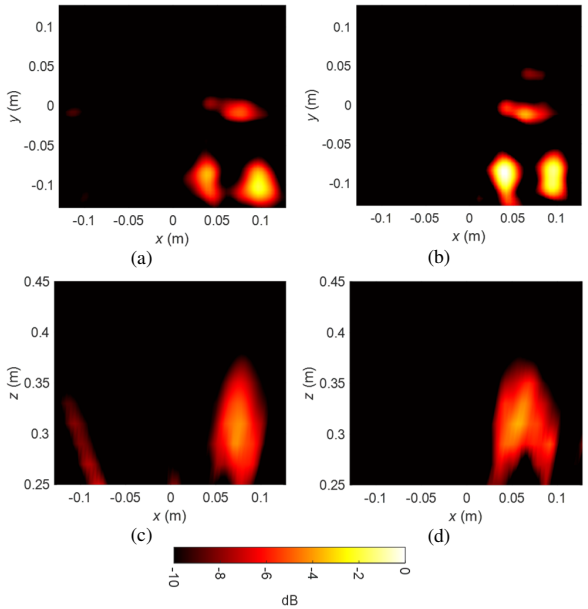

Fig. 6. Reconstructed image of the target in the 18-19 GHz frequency band and with $m_f = 26$; (a) at $z = 33\text{cm}$ and using the MF method, (b) at $z = 33\text{cm}$ and using the LS method with $n_i = 30$, (c) at $y = 0$ and using the MF method, (d) at $y = 0$ and using the LS method with $n_i = 30$.

It is worth noting that the reason why the upper stripe is seen as smaller in all images (despite the similar size of all stripes) is related to the configuration of the DMAs and the position of the stripes relative to it (see Fig. 2). By considering

the configuration of the DMAs, it is clear that the power distribution is maximum in the lower right corner (closer to the intersection of the TX and RX DMAs) and the further away from there, the less power is received.

V. Conclusion

This study experimentally validated a computational imaging system based on DMAs arranged in an L-shaped configuration. The results highlighted the impact of key system parameters, such as the number of masks, frequency samples, and reconstruction algorithms, on the final imaging performance. Increasing the number of masks significantly improved image fidelity, as more measurement modes enhanced spatial diversity. Similarly, a higher number of frequency samples resulted in better depth resolution, whereas reducing the bandwidth degraded the range resolution. Comparative evaluations between the MF and LS reconstructions confirmed that while the MF method provides rapid results, the LS method (particularly with iterative solvers) yields superior image quality at the cost of increased computational time. The study demonstrated the feasibility of DMA-based CI systems for real-world applications, offering a scalable and efficient alternative to conventional microwave imaging techniques. Future work will explore further optimizations, including real-time processing and advanced regularization techniques, to enhance performance in practical imaging scenarios.

References

[1] S. Hassani and U. Dackermann, "A systematic review of advanced sensor technologies for non-destructive testing and structural health monitoring," *Sensors,* vol. 23, no. 4, p. 2204, 2023.

[2] V. Vasagar *et al.*, "Non-destructive techniques for corrosion detection: A review," *Corrosion Engineering, Science and Technology,* vol. 59, no. 1, pp. 56-85, 2024.

[3] R. Fakhlaei *et al.*, "Application, challenges and future prospects of recent nondestructive techniques based on the electromagnetic spectrum in food quality and safety," *Food Chemistry,* p. 138402, 2024.

[4] A. M. Molaei, S. Hu, V. Skouroliakou, V. Fusco, X. Chen, and O. Yurduseven, "Fast processing approach for near-field terahertz imaging with linear sparse periodic array," *IEEE Sensors Journal,* vol. 22, no. 5, pp. 4410-4424, 2022.

[5] O. Yurduseven, "Indirect microwave holographic imaging of concealed ordnance for airport security imaging systems," *Progress in Electromagnetics Research,* vol. 146, pp. 7-13, 2014.

[6] M. A. Assou, "Synthetic aperture imaging and spectroscopy in the terahertz range using time domain spectroscopy system," Université de Limoges, 2024.

[7] P. A. Molchanov, *Seeing Invisible: Advanced Antenna Arrays*. CRC Press, 2024.

[8] M. Zhao, S. Zhu, R. Sharma, A. M. Molaei, X. Chen, and O. Yurduseven, "Metamaterial Iris-Based Cavity Antenna for mm-Wave Computational Polarimetric Imaging," *IEEE Antennas and Wireless Propagation Letters,* vol. 23, no. 11, pp. 3367-3371, 2024.

[9] O. Yurduseven, T. Fromenteze, K. Cooper, G. Chattopadhyay, and D. R. Smith, "From microwaves to submillimeter waves: modern advances in computational imaging, radar, and future trends," in *Terahertz, RF, Millimeter, and Submillimeter-Wave Technology and Applications XII*, 2019, vol. 10917: SPIE, pp. 134-144.

[10] M. Zhao *et al.*, "Dual-polarized frequency-diverse metaimager for computational polarimetric imaging," *IEEE Transactions on Antennas and Propagation,* 2024.

[11] A. Jabbar *et al.*, "60 GHz Programmable Dynamic Metasurface Antenna (DMA) for Next-Generation Communication, Sensing, and Imaging Applications: From Concept to Prototype," *IEEE Open Journal of Antennas and Propagation,* 2024.

[12] A. M. Molaei *et al.*, "Near-Field Bistatic Microwave Imaging with Dynamic Metasurface Antennas," in *2024 18th European Conference on Antennas and Propagation (EuCAP)*, 2024: IEEE, pp. 1-5.

[13] A. M. Molaei *et al.*, "Application of Kirchhoff Migration Principle for Hardware-Efficient Near-Field Radar Imaging," *IEEE Transactions on Computational Imaging,* vol. 10, pp. 1000-1015, 2024.

[14] F. Dai, S. Zhang, L. Li, and H. Liu, "Enhancement of metasurface aperture microwave imaging via information-theoretic waveform optimization," *IEEE Transactions on Geoscience and Remote Sensing,* vol. 60, pp. 1-12, 2022.

[15] V. Skouroliakou, A. M. Molaei, M. Garcia-Fernandez, G. Alvarez-Narciandi, and O. Yurduseven, "A case study of misalignment errors for range-migration-based microwave imaging with multistatic dynamic metasurface apertures," in *2024 18th European Conference on Antennas and Propagation (EuCAP)*, 2024: IEEE, pp. 1-5.

[16] A. M. Molaei *et al.*, "Development of fast Fourier-compatible image reconstruction for 3D near-field bistatic microwave imaging with dynamic metasurface antennas," *IEEE Transactions on Vehicular Technology,* vol. 71, no. 12, pp. 13077-13090, 2022.

[17] A. M. Molaei, V. Skouroliakou, V. Fusco, and O. Yurduseven, "Efficient 3D image reconstruction for near-field microwave imaging using dynamic metasurface antenna," *IEEE Access,* vol. 10, pp. 68491-68498, 2022.

[18] V. Skouroliakou, A. M. Molaei, and O. Yurduseven, "Towards real-time three-dimensional (3D) imaging using dynamic metasurface antennas," in *2023 17th European Conference on Antennas and Propagation (EuCAP)*, 2023: IEEE, pp. 1-5.

[19] G. Álvarez-Narciandi, M. García-Fernández, V. Skouroliakou, and O. Yurduseven, "Dynamic Metasurface Antenna-Based Mills-Cross Aperture for 3-D Computational Microwave Imaging," *IEEE Antennas and Wireless Propagation Letters,* vol. 23, no. 11, pp. 3377-3381, 2024.

[20] G. Alvarez-Narciandi, M. Garcia-Fernandez, and O. Yurduseven, "Impact of the Unit Cell Distribution of 1-D Dynamic Metasurface Antennas on the Performance of a Computational Imaging System," in *2024 18th European Conference on Antennas and Propagation (EuCAP)*, 2024: IEEE, pp. 1-5.

[21] R. Peng, "Deep Learning Assisted Large Scale Metamaterial Simulation," Duke University, 2024.

[22] G. Lipworth *et al.*, "Comprehensive simulation platform for a metamaterial imaging system," *Applied optics,* vol. 54, no. 31, pp. 9343-9353, 2015.

[23] H. Armeshi, M. R. Sahebi, and H. Aghababaei, "A deterministic descriptive regularization-based method for SAR tomography in urban areas," *International Journal of Remote Sensing,* vol. 45, no. 6, pp. 1884-1903, 2024.

[24] T. V. Hoang *et al.*, "Spatial diversity improvement in frequency-diverse computational imaging with a multi-port antenna," *Results in Physics,* vol. 22, p. 103906, 2021.

[25] M. Pasha, A. K. Saibaba, S. Gazzola, M. I. Español, and E. de Sturler, "A computational framework for edge-preserving regularization in dynamic inverse problems," *Electronic Transactions on Numerical Analysis,* vol. 58, pp. 486-516, 2023.

[26] W. Lu, "Advanced regularization and discretization methods in diffuse optical tomography," University of Birmingham, 2020.

[27] M. Sedlacek, "Sparse approximate inverses for preconditioning, smoothing, and regularization," Technische Universität München, 2012.

[28] O. Yurduseven, T. Fromenteze, C. Decroze, and V. F. Fusco, "Frequency-Diverse Computational Automotive Radar Technique for Debris Detection," *IEEE Sensors Journal,* vol. 20, no. 22, pp. 13167-13177, 2020.

[29] D. L. Sun, T. Z. Huang, Y. F. Jing, and B. Carpentieri, "A block GMRES method with deflated restarting for solving linear systems with multiple shifts and multiple right-hand sides," *Numerical Linear Algebra with Applications,* vol. 25, no. 5, p. e2148, 2018.

[30] A. M. Molaei, S. Hu, V. Skouroliakou, V. Fusco, X. Chen, and O. Yurduseven, "Fourier compatible near-field multiple-input multiple-output terahertz imaging with sparse non-uniform apertures," *IEEE Access,* vol. 9, pp. 157278-157294, 2021.